Biophysical Reports

ARTICLE

Tunable intracellular transport on converging microtubule morphologies

Niranjan Sarpangala,[1] Brooke Randell,[2] Ajay Gopinathan,[3] and Oleg Kogan[4,*]
[1]University of Pennsylvania, Philadelphia, Pennsylvania; [2]University of California, Santa Cruz, Santa Cruz, California; [3]University of California, Merced, California; and [4]Queens College of CUNY, Queens, New York

ABSTRACT A common type of cytoskeletal morphology involves multiple microtubules converging with their minus ends at the microtubule organizing center (MTOC). The cargo-motor complex will experience ballistic transport when bound to microtubules or diffusive transport when unbound. This machinery allows for sequestering and subsequent dispersal of dynein-transported cargo. The general principles governing dynamics, efficiency, and tunability of such transport in the MTOC vicinity are not fully understood. To address this, we develop a one-dimensional model that includes advective transport toward an attractor (such as the MTOC) and diffusive transport that allows particles to reach absorbing boundaries (such as cellular membranes). We calculated the mean first passage time (MFPT) for cargo to reach the boundaries as a measure of the effectiveness of sequestering (large MFPT) and diffusive dispersal (low MFPT). We show that the MFPT experiences a dramatic growth, transitioning from a low to high MFPT regime (dispersal to sequestering) over a window of cargo on-/off-rates that is close to in vivo values. Furthermore, increasing either the on-rate (attachment) or off-rate (detachment) can result in optimal dispersal when the attractor is placed asymmetrically. Finally, we also describe a regime of rare events where the MFPT scales exponentially with motor velocity and the escape location becomes exponentially sensitive to the attractor positioning. Our results suggest that structures such as the MTOC allow for the sensitive control of the spatial and temporal features of transport and corresponding function under physiological conditions.

WHY IT MATTERS We develop a one-dimensional, two-layer model to study the dynamics, efficiency, and tunability of intracellular transport in the vicinity of converging microtubule morphologies. Our work draws attention to the idea of an optimal parameter regime for tunability of cell transport properties, allowing cells to achieve large changes in the functionality—such as the transport time or exit location preference—by changing regulatory parameters, such as the cargo to microtubule on-/off-rate or the position of the microtubule convergence. We find that in vivo values correspond to parameters that maximize the sensitivity—possibly ensuring easy tunability of cell function with relatively small adjustments of transport parameters or organelle positioning.

INTRODUCTION

The transport of material within eukaryotic cells is a critically important physiological process that cannot be achieved by passive diffusion alone. In these cells, cargo, including vesicles and organelles, is dragged along by a variety of molecular motors that utilize energy from ATP hydrolysis to power their directed stepping motion along cytoskeletal protein filaments with a well-defined polarity (1). Motors from different families such as kinesins and myosins step along different filaments (microtubules (MTs) and actin respectively), and others such as dynein move along the same MT filaments as kinesins but in the opposite direction. Transport at the cellular scale is therefore a complex process that involves phases of multiple motors effecting directed transport along cytoskeletal filament networks interspersed with passive diffusion of the cargo (2, 3). This process is essential for the transport of a variety of cargos between specific locations and organelles within the cell. Examples include the transport of cargo in cilia (4), between the plasma membrane and Golgi apparatus (5), (6), between endoplasmic reticulum and Golgi (7), (3), transport of viruses toward replication sites (8), (9), and the transport of many other vesicles

---

Submitted June 18, 2024, and accepted for publication July 5, 2024.
*Correspondence: oleg.kogan@qc.cuny.edu
Editor: Jorg Enderlein.
https://doi.org/10.1016/j.bpr.2024.100171

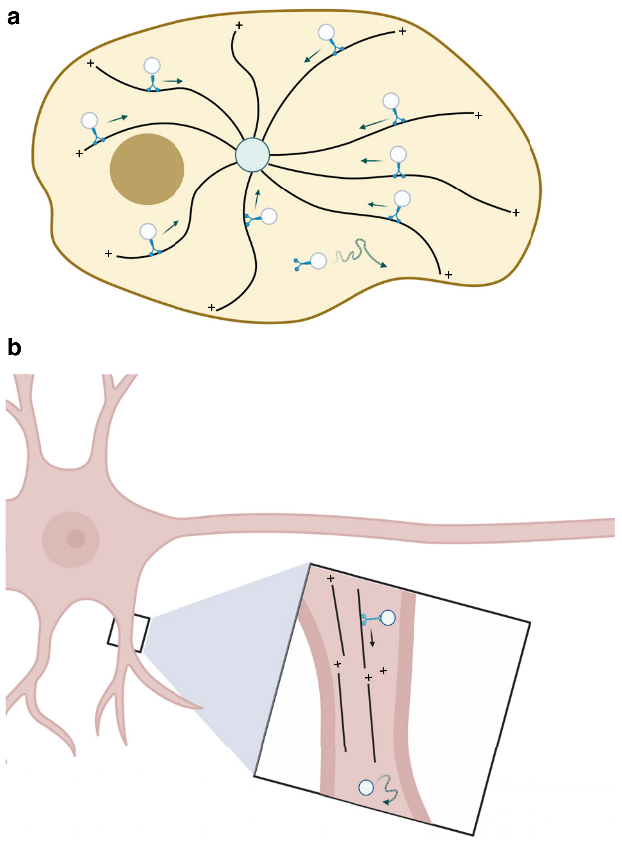

FIGURE 1 (*a*) A model of a cell in which microtubules have a strong central organization, with minus ends at the centrosome. A dark circle represents an organelle. Dynein motors are shown moving on microtubules. (*b*) One-dimensional morphology found in dendrites. Here, the ends of the same polarity from different microtubules can face each other. This schematic is based on (20). Created with BioRender.com.

and organelles for various functional purposes (see review (3)) (10).

Much like the design of road networks affects traffic flow, the morphologies of the cytoskeletal networks in cells have been shown to have a significant effect on intracellular transport (11–14). This is particularly important as even a single type of cytoskeletal filament, such as MTs, exhibits a wide diversity of morphologies within different cell types to enable different functions (15). In some situations, such as in melanophores, MTs have a strongly ordered (in this case radial) organization (16). In others, the orientation or polarity of MT morphology can be broadly distributed. In pancreatic β-cells, for example, MTs are arranged with both an orientational and polarity disorder (17), although there is an average polarity. On the other hand, MTs in neuronal dendrites are essentially aligned with the long direction of the dendrite, but their polarity is not uniform (18), resulting in junctions of plus or minus ends along the dendrite.

A common structural feature that governs these MT morphologies is the microtubule organizing center (MTOC) that is responsible for growing MTs and localizing and stabilizing their minus ends, leading to multiple MTs converging with their minus ends at the MTOC (15). Dynein-driven transport along MTs will move cargo to the vicinity of MTOC, whereas kinesin mediated transport moves cargo away from it. These ballistic phases are interspersed with isotropic diffusion for unbound cargo-motor complexes.

The spatial and temporal positioning of the MTOC therefore allows for transport of some types of cargo toward and other types of cargo away from specific organelles that can act as MTOCs as well as locations within the cell in the vicinity of the MTOC. The centrosome is an organelle that often serves as an MTOC especially during mitosis, and it is typically positioned in the proximity of the nucleus (Fig. 1 *a*). Centrosomes can therefore enable radial transport in both directions such as kinesin-mediated secretory vesicle transport and the dynein-mediated transport of endocytic vesicles and even some viruses toward the nuclear envelope (8,9). However, in many differentiated cells, other noncentrosomal locations and organelles can also serve as MTOCs (19). This is important for generating nonradial morphologies that can provide specific structural support or transport directionality. For example, epithelial cells in many species have apically located MTOCs that generate an apical-basal orientation of MTs (19), whereas Golgi and mitochondria have also been reported to perform as MTOCs in many cell types (5,6,19).

It is also possible to switch between different modes of transport of the same cargo with the same MT morphology by changing motor types or kinetics. For example, in melanophores (16,21), a perinuclear MTOC produces a radial MT structure with minus ends in toward the nucleus and plus ends out toward the membrane. Cells achieve color change by aggregating and sequestering pigment containing melanosomes near the nucleus via ballistic dynein-mediated transport. Upon hormonal stimulation, they can switch to a superdiffusive dispersal phase powered by a combination of kinesin and actin.

In some cases, rather than aggregation or dispersal, cargo needs to traverse regions with convergent MT morphologies. Such cases occur in dendritic processes of neuronal cells that have been shown to have regions of alternating polarity of MTs (18) (Fig. 1 *b*). Directed transport of dynein (kinesin) carrying cargo at a junction of multiple minus ends (multiple plus ends) will have to overcome what is essentially a trap to maintain observed unidirectional transport toward or away from the main cell body (18).

Finally, the location of MTOCs can also be tuned over time to accommodate different cellular functions

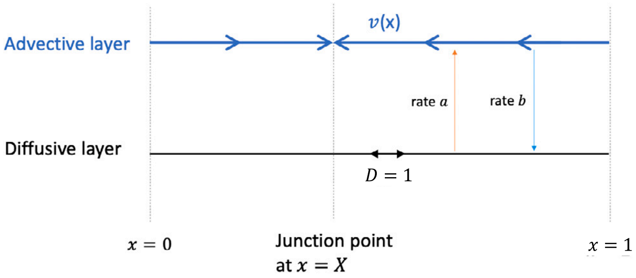

FIGURE 2 One-dimensional model with dimensionless parameters.

such as sequestering and dispersal of cargo. An example occurs in lymphocytes that enable cytotoxicity by secreting the contents of lysosomes (lytic granules) at the immunological synapse to kill the target cell. Here, dynein-dependent sequestering of the lytic granules at the MTOC occurs rapidly, followed by the gradual movement of the MTOC toward the synapse with subsequent secretion (22,23).

In all these cases, it is important to understand the dynamics of the transport and its sensitivity to biological parameters in order to understand functional efficiency and robustness. In particular, given the wide variety of functional contexts in which the converging MT geometry facilitates transport, it is critical to understand the general principles governing dynamics, efficiency, and tunability of such transport in the MTOC vicinity.

To address this gap, we develop a simple one-dimensional model that includes advective transport toward an attractor (such as the MTOC) and diffusive transport that allows particles to reach absorbing boundaries (such as cellular membranes). This can be viewed as a two-layer model consisting of an advective layer (AL) endowed with an attractor, a diffusive layer (DL), and absorbing boundaries along the perimeter of the domain (see Fig. 2). The number of independent control parameters in this problem can be reduced to four. These are the rates of attachment to and detachment from MTs, advective velocity, and the placement of the attractor within the domain. We take the residence time, or more precisely, the mean first passage time (MFPT), for cargo to reach the boundaries as a measure of the effectiveness of sequestering or directed transport (large MFPT) and diffusive dispersal (low MFPT). In other words, given an initial location of the cargo within the domain (determined by the placement of the source of cargo, e.g., an organelle), this quantity tells the average time to reach either of the absorbing boundaries (i.e., escape the domain, e.g., the cell) or a specific boundary (in one dimension, left or right). Another relevant quantity is the probability of escape through one or the other boundary.

Using this model, we were able to make a series of physiologically relevant predictions—on which we report here.

Symmetric, or nearly symmetric, attractor positions (centrosomal MTOCs near the nuclei for example) can give rise to a significant increase in the value of MFPT—thus switching from disperal to trapping—within a certain range of dimensionless on-/off-rates. Concurrently with this rise of MFPT, the probability to escape purely diffusively goes to zero in the same range of (dimensionless) on-/off-rates. This means that for larger on-/off-rates, any cargo particle will have to experience at least one episode of motion on MTs. Interestingly, biophysical parameters in cells correspond to this range of dimensionless on-/off-rates, suggesting that cells can access the full range of MFPT regimes (from dispersal to trapping).

Second, when the attractor is positioned asymmetrically (off-center) in the domain, representing noncentrosomal MTOCs for example, we predict the existence of optimal on- or off-rates that minimize the MFPT. This suggests that rates could be tuned in cells to achieve fast, targeted delivery of cargo that needs to be gathered first, such as the case of lytic granules in lymphocytes discussed above. It is to be noted that a similar optimization has been predicted in the study of diffusion with stochastic reset (24), (25). Indeed, attachment to the MT, followed by a rapid transport to the attractor, followed by detachment from the MT back to diffusion in the cytoplasm is effectively a reset.

When the on-/off-rate is much larger than all other rates in the problem, the model reduces to an effectively one-layer system. Here, we demonstrate that even a slight asymmetry in the position of the attractor can lead to a very strong amplification of the preferred exit end. This provides an example of sensitivity to small parameter changes—in this case asymmetric of the attractor placement—an effect that can be exploited by cells with noncentrosomal MTOCs or by dynamically repositioning MTOCs to select a preferred location for cargo to be targeted to.

It is to be noted that cellular transport typically takes place in two and three dimensions, whereas our mathematical analysis is based on a one-dimensional model. This approximation allows us to solve the problem analytically and shed light on qualitative features of the problem. Additionally, there are scenarios that are genuinely one-dimensional such as in neuronal dendrites that we discussed above. Dendrites are much larger in length than they are in diameter (26), and MTs are typically aligned along the long axis of a dendrite. Thus, transport in dendrites is effectively a one-dimensional process. Moreover, as discussed above, dendritic MTs have regions of alternating polarity of MTs (18), resulting in advection toward a central junction, a setting that matches our one-dimensional model. Although the main goal of this paper is to theoretically identify ranges of parameters corresponding to different functional regimes such as aggregation and dispersal and the sensitivity to parameters in these regimes, specific examples of cell types operating in each parameter regime will also be discussed.

MATERIALS AND METHODS

Model

We consider the minimal model in a one-dimensional domain of length L. It contains an AL that represents motion along MTs and a DL that represents diffusion in the cytoplasm. We assume that attachment to and detachment from MTs are Poisson processes, endowed with rates α and β, respectively. This means, for example, that a motor spends on average a time $1/\beta$ advecting after attaching to an MT. While advecting on the AL, particles move with a uniform velocity toward an attracting fixed point (or attractor) located at some coordinate $x = X_0$ between $x = 0$ and $x = L$ (see Fig. 2). The region of length L serves as a domain of attraction for the attractor at $x = X_0$. For example, in linear geometries like dendrites, two successive regions with alternating polarity of MTs (junctions of plus ends or minus ends facing each other) would be a domain of attraction for the intervening junction, whereas for radial geometries, the entire cell can serve as a domain of attraction for dynein-transported cargo to the centrosome. We wish to compute the time evolution of the cargo density within the domain of attraction, which allows us to calculate other related quantities such as currents, the MFPT, and likelihood of exit at each end.

Letting $\rho(x)$ and $\theta(x)$ be probability densities of particles in the AL and DL, respectively, the dynamics are given by

$$\frac{\partial \rho}{\partial t} = -\frac{\partial}{\partial x}(v(x)\rho) + \alpha\theta - \beta\rho \tag{1}$$

$$\frac{\partial \theta}{\partial t} = -\alpha\theta + \beta\rho + D\frac{\partial^2 \theta}{\partial x^2} \tag{2}$$

on $0 \le x \le L$. The velocity field is given by

$$v(x) = \begin{cases} +v_0 \ldots x < X_0 \\ -v_0 \ldots x > X_0 \end{cases} \tag{3}$$

The parameters are the attachment and detachment rates α and β, the diffusion coefficient D, the advective velocity on MTs v_0, and the location of the attractor X_0. There are absorbing boundary conditions at $x = 0$ and $x = L$, i.e., $\rho(0) = \theta(0) = 0$ and $\rho(L) = \theta(L) = 0$, corresponding to a permanent exit from the domain. Altogether, there are six physical parameters.

We switch to dimensionless variables by rescaling the lengths by L and times by L^2/D. Thus, $x' = x/L$ and $t' = tD/L^2$. The resulting equations are

$$\frac{\partial \rho}{\partial t'} = -\frac{\partial}{\partial x'}(v'(x')\rho) + a\theta - b\rho \tag{4}$$

$$\frac{\partial \theta}{\partial t'} = -a\theta + b\rho + \frac{\partial^2 \theta}{\partial x'^2} \tag{5}$$

on $0 < x' < 1$, with $\rho(0) = \theta(0) = 0$ and $\rho(1) = \theta(1) = 0$, the velocity field

$$v'(x') = \begin{cases} +v \ldots x' < X \\ -v \ldots x' > X \end{cases},$$

where $X = X_0/L$, $v = \frac{v_0 L}{D}$, $a = \frac{\alpha L^2}{D}$ (on-rate), and $b = \frac{\beta L^2}{D}$ (off-rate). From now on, $x, t,$ and v will refer to the dimensionless variables. The model is depicted schematically in Fig. 2.

Range of parameters

Here, we review the values of parameters from the literature. The order of magnitude of both the on-rate α and off-rate β are expected to be of the order of 1 per second. For example, (11) cites $\beta = 1\ s^{-1}$, whereas (27) reports $\beta = 1\ s^{-1}$ for kinesin-1 and $0.25\ s^{-1}$ for cytoplasmic dynein. Off-rates also depend on ATP concentration (28). The calculation of on-rates of cargo is nuanced, as it involves the number of motors that are attached to cargo, their diffusion coefficient on the cargo, and the proximity of a motor to the MT. These issues are discussed in (28) and references therein; see also (29). The source (27) reports $\alpha = 5\ s^{-1}$ for kinesin-1 and $1.5\ s^{-1}$ for cytoplasmic dynein. The work (30) report kinesin on-rates $4.7 \pm 2.4\ s^{-1}$, measured experimentally, and they cite another experimental measurement of kinesin average off-rates to be $0.42\ s^{-1}$ in the absence of cargo. Overall, the order of magnitude of $1\ s^{-1}$ is a reasonable estimate for both the on- and off-rates. MT lengths typically fall in the range of $1 - 10\ \mu m$ (11). This is consistent with in vivo studies (31) and predictions of theoretical models (32). However, the length of advective path may be much larger. For example, in neurons, a cargo that needs to be delivered from the soma to synapses on the ends of axons will travel a length of the order of a meter (3). The velocity of molecular motors on MTs is on the order of $1\ \mu m/s$ (3), (11), (27), although this quantity also has a degree of variability (33), (34). Diffusion coefficient of vesicular organelles in the cytoplasm fall in the range $10^{-3} - 10^{-1}\ \mu m^2/s$ (3). Similar values of parameters are reported in the theoretical paper by Smith and Simmons (35). It deserves to be mentioned that most of these parameters come from in vitro studies. Indeed, obtaining parameters in vivo is a notoriously difficult task. Having said this, our results do not depend on exact values of real parameter values. Rather, our goal is to predict what (in vivo) parameter regions correspond to different behaviors (for example, sequestering of cargo versus easy dispersal of cargo).

Given these physical parameters, our dimensionless parameters a and b will take on values in the range $[10, 10^5]$, and parameter v will take on values in the range $[10, 10^4]$. There are four timescales in the problem: $1/a$, $1/b$, the advective timescale $1/v$, and the diffusive timescale (which is of order 1 in dimensionless units). Different special cases or behavioral regimes emerge when one of these timescales differs significantly from the others. The limit that is particularly amenable to analysis is one in which $1/a$ and $1/b$ are both much smaller than the advective time (which is of order $1/v$ in dimensionless units) and diffusive time (which is of order 1 in dimensionless units). We will formally call it the $a, b \to \infty$ limit.

Analytical approach in the one-layer limit

A very important special case is $a = b$. As $a = b \to \infty$, the model reduces to an effective one-layer model:

$$\frac{\partial P}{\partial t} = -\frac{\partial}{\partial x}\left(v(x)P(x) - \frac{\partial P}{\partial x}\right), \tag{6}$$

where $P(x,t)$ is the probability density (i.e., P describes both θ and ρ, which become identical). A general solution will be written as an eigenfunction expansion:

$$P(x,t) = \sum_n c_n p_n(x) e^{\sigma_n t}, \tag{7}$$

where $p_n(x)$ and σ_n are nth eigenfunction and eigenvalue, which satisfy $Op_n = \sigma_n p_n$, with the operator O given by

$$O = -\frac{\partial}{\partial x}\left(v(x) - \frac{\partial}{\partial x}\right), \tag{8}$$

with

$$v(x) = \begin{cases} +v \ldots x < X \\ -v \ldots x > X \end{cases} \tag{9}$$

and a constant v. Thus, the one-layer model contains two parameters: dimensionless advective velocity v and dimensionless position of the attractor X, which can take on values between 0 and 1.

The computation of eigenvalues σ_n and eigenfunctions $p_n(x)$ of the operator O, as well as the computation of the eigenfunctions $q_n(x)$ of the adjoint operator $O^\dagger$, is given in Supporting Material B.

Starting from the initial condition $P(x, t = 0) = \delta(x - x_0)$, the probability density will be given by

$$P(x,t;x_0) = \sum_n \frac{q_n^*(x_0) p_n(x)}{\int_0^1 q_n^*(x') p_n(x')\, dx'} e^{\sigma_n t} \tag{10}$$

The MFPT can be extracted from this probability density, but P contains more information than just the MFPT.

To calculate the MFPT $\tau(x_0)$, we notice that the magnitude of the current through the boundary is given by $f(t) = \left|\frac{\partial P}{\partial x}\right|_{bdry}$ in dimensionless units. Then $f(t)dt$ gives the fraction of initial particles that cross the boundary in the time interval $[t, t+dt]$ = probability of crossing that boundary in $[t, t+dt]$, since the initial condition is normalized to 1. So, $p = \int_0^\infty f(t)\, dt$ gives the probability of ever leaving through that boundary, $\frac{f(t)dt}{p}$ gives the probability that particles that leave through that boundary do so in $[t, t+dt]$, and finally $\tau = \int_0^\infty t \frac{f(t)}{p}\, dt$ is the average time to leave through that boundary, i.e., MFPT conditioned on that particular boundary. In this problem, there are two boundaries, with τ_l and τ_r denoting MFPT to exit through the left and the right boundary, respectively. We expect $\tau_l \to 0$ as $x_0 \to 0$ and $\tau_r \to 0$ as $x_0 \to 1$. Finally, MFPT in general—without conditioning on a specific boundary—is the weighted average of the two: $\tau = \tau_l p_l + \tau_r p_r$, which matches predictions using other methods (36).

We note in passing that in situations in which the ratio a/b is fixed at a value $\neq 1$ (for example, $a = 2b$), two-layer predictions in the $a \to \infty$ limit don't reduce to the one-layer model; by controlling the ratio of a/b, we control the relative importance of advection versus diffusion, but such a control knob is not present in Eq. (6). We found, however, that the $a \to \infty$ limit of the two-layer model with a fixed ratio a/b is approximately captured by the one-layer theory with a velocity suppressed by a factor a/b; see Supporting Material H.

Analytical approach in the general case

To analyze the full two-layer model, we again seek a general solution (to Eqs. (4) and (5)) via an eigenfunction expansion of the form

$$\begin{pmatrix} \rho(x,t) \\ \theta(x,t) \end{pmatrix} = \sum_n c_n \begin{pmatrix} R_n(x) \\ \Theta_n(x) \end{pmatrix} e^{-\sigma_n t} \tag{11}$$

(we found it convenient to factor out the negative sign from σ here), where $\begin{pmatrix} R_n \\ \Theta_n \end{pmatrix}$ and σ_n are the nth (vector) eigenfunction and eigenvalue, which satisfy $O\begin{pmatrix} R_n \\ \Theta_n \end{pmatrix} = \sigma_n \begin{pmatrix} R_n \\ \Theta_n \end{pmatrix}$, with the operator O now given by

$$O = \begin{pmatrix} \frac{\partial}{\partial x} v(x) + b & -a \\ -b & a - \frac{\partial^2}{\partial x^2} \end{pmatrix} \tag{12}$$

and $v(x)$ given by Eq. (9). The full model contains four parameters: dimensionless advective velocity v, dimensionless rates a and b, and dimensionless position of the attractor X, which can take on values between 0 and 1. The computation of eigenvalues and eigenfunctions is provided in Supporting Material A.

Remarkably, there are only a finite number of eigenfunctions and eigenvalues. In other words, the eigenset is not complete. As $a = b \to \infty$, this number goes to infinity, whereas the lower-lying eigenvalues and eigenfunctions approach those of the one-layer model. The completeness is not guaranteed, since the operator O is not Hermitian. Thus, an expansion such as in Eq. (11) is of limited use and cannot be used to fit a solution for an arbitrary initial condition—including a point-like δ function initial condition. This also implies that we cannot compute escape currents and MFPT from such initial conditions. The distribution exists, but it cannot be found using the methods used here.

However, we can always compute the ground-state eigenvalue, σ_1. Then, the time $1/\sigma_1$—although not a true MFPT—is an estimate of a characteristic time for escape. This estimation should become more accurate as escape events become rare (MFPT $\gg$ than all other timescales)—for example, when v is sufficiently large. In the rare event regime, the gap between σ_1 and σ_2 is much larger than the gap between all other eigenvalues. Therefore, higher eigenmodes contribute little to the probability current in the rare event limit. Moreover, although this calculation does not give IC dependence, MFPT loses this dependence as escape events become rare, since the system will, with overwhelming probability, first visit the attractor following the initial location before escaping through boundaries. We found that in practice the estimation $1/\sigma_1$ agrees with MFPT computed in simulations quite well over a wide range of parameters. So, when it comes to the general a and b cases, we will state $1/\sigma_1$ as analytical estimates of MFPT.

Monte Carlo simulation method

We considered a simple one-dimensional computational model to simulate the transport process in a domain of length L with attractor formed by oppositely oriented MTs. Our computational model involves two layers, an AL where the particle undergoes active transport and a DL where it does a one-dimensional random walk. We consider one particle at a time. To begin, we initialize the particle at position $x = x_0$ within the domain $x \in [0, L = 1]$ either in the DL or in AL as required. We consider that the particle can switch from DL to AL with a rate a and from AL to DL with a rate b. When a particle switches to DL, a time t_d is drawn from the exponential distribution e^{-at}, and the particle is allowed to diffuse for $n = t_d/\Delta t$ number of steps. Δt is the time step in the simulation. In each step, the position is updated as

$$x(t + \Delta t) = x(t) + r\Delta x, \tag{13}$$

where r is drawn from the set $\{-1, 0, 1\}$ with the probability $p = 1/3$. Δx is the step size that is chosen such that the diffusion

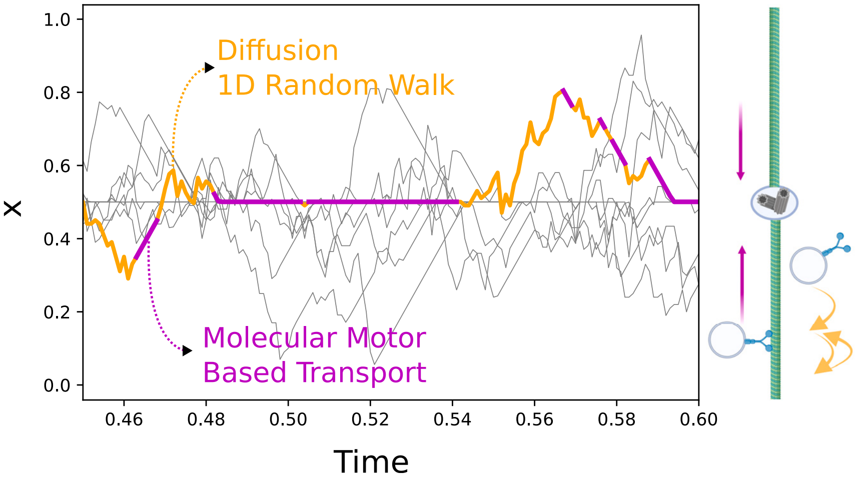

FIGURE 3 A sample trajectory generated by the Monte Carlo simulation. Diffusive motion is indicated with an orange line, and advective motion with a magenta line. Gray colored lines indicate more sample trajectories. Here, $X = 0.5$. Cartoon created with BioRender.com.

constant of the particle $D = \frac{p\Delta x^2}{\Delta t}$ is 1. Right after finishing a diffusive portion of a simulation run, the particle switches from DL to AL. In the AL, the particle stays for a time t_a drawn from e^{-bt}, i.e., $n = t_a/\Delta t$ number of steps. The position of the particle in the AL is updated as

$$x(t+\Delta t) = x(t) + v(x)\Delta t, \tag{14}$$

where $v(x)$ is the advective velocity given by Eq. (9). These alternative portions of a simulation run in DLs and ALs are continued until the particle reaches one of the boundaries ($x = 0$ or $x = 1$) or until maximum simulation time, T_{max} is reached. We then repeat with N particles to get enough statistics to calculate the overall MFPT, probabilities and MFPTs to exit out of specific boundaries, and other quantities.

Trajectories

To get the trajectories, we record the data of the x position and the layer in which particle is located at regular time intervals during each simulation run.

An example of trajectories is shown in Fig. 3.

Computation of net MFPT

To compute the net MFPT for a given parameter set, we perform simulation runs until the particle exits out of one of the boundaries ($x = 0$ or $x = 1$) or until $t = T_{max}$. We record the time of exit for each run and then compute the mean and standard error of the mean for all N runs. Standard error of mean is computed as the standard deviation divided by the square root of sample size (scipy.stats.sem).

Computation of conditional MFPT and escape probability

To compute the MFPT for exit specifically through the left (or the right) boundary, we record the time as well as the boundary through which the particle exits. Then, we filter out only those simulation runs where a particle exited out of the left (or right) boundary. Then, we compute the mean and standard error of the mean for those runs. We compute the escape probability through left (or right) boundary as the fraction of runs that exited out of the left (or right) boundary.

Statistics of visits to the AL

We measure the fraction of simulation runs in which a particle that started on the DL ended up making at least one visit to the AL. In each simulation run, we also compute the number of visits to the AL before exiting. To do this, we update a counter every time the particle switches from the DL to the AL. We then compute the average over N runs.

RESULTS AND DISCUSSION

Variation of the on-/off-rate can change escape times by orders of magnitude

This problem has many parameters, so we present important special cases first in order to make sense of the results. To do that, we start with the symmetric case, $X = 1/2$, and we set the particles' initial placement also in the middle, i.e., $x_0 = 1/2$ (this is the initial condition). We will also let $a = b$ for now. Although the on- and off-rates are generally not identical, they are typically of the same order of magnitude. Unequal on- and off-rates will be discussed next. We will use the term "switching rate" to refer to on- or off-rates in the $a = b$ situation, and we denote both rates by the letter s that stands for switching rate.

Panels (a) and (b) of Fig. 4 display the MFPT as a function of s at different advective speeds v on a logarithmic scale; panel (a) is for initial placement on the AL (MT), whereas panel (b) is for initial placement on the DL (cytoplasm). The MFPT is in dimensionless time units. Dimensionless switching time of 1 (so, s is also 1) means the timescale for switching between layers is the same as the timescale to diffuse over the domain length. To convert to time in seconds, we multiply by L^2/D expressed in physical units. For example, for $L = 1$ μm and $= 10^{-2}$ $\mu m^2/s$, the MFPT of 10 dimensionless time units corresponds to 10^3 seconds. To help understand the physics of the process, we also plot, in panel (c), the fraction of times that particles initially placed on the DL visit the AL, as well as the number of times they do so in panel (d) (also when starting on DL).

We call the reader's attention to panel (a) of Fig. 4 —the plot of MFPT versus s for AL initial condition.

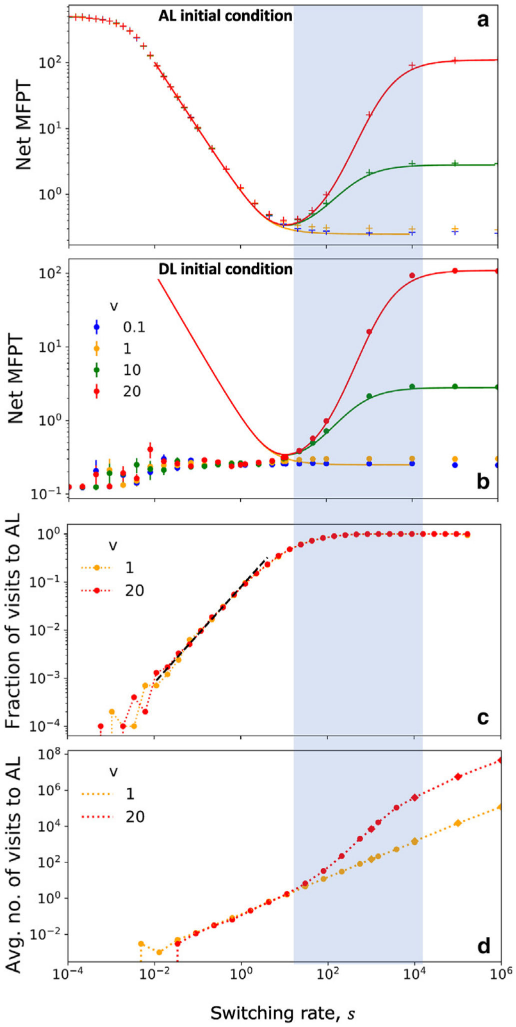

FIGURE 4 Symmetric case: $X = 0.5$, where the initial location of particles is also at $x_0 = 0.5$. (*a*) MFPT versus s with initial condition (IC) on the AL. (*b*) MFPT versus s with IC on the DL. Dots and crosses are simulation results; solid curves are analytical estimations of MFPT given by $1/\sigma_1$. The MFPT is in dimensionless time units. To convert to time in seconds, we multiply by L^2/D expressed in physical units. The last two points ($a = 10^5$ and 10^6) required a smaller $dt = \frac{10^{-6}}{3}$; $dt = \frac{10^{-4}}{3}$ was sufficient for the rest. Therefore, we used $N = 10^3$ for the last two points to optimize simulation time and $N = 10^4$ for the rest. Error bars for MFPT represent the standard error of mean. (*c*) Fraction of simulation runs that visit the AL at least once after starting in the DL. The dashed line is a fit of the form $0.079a$. Here, $N = 10^4$ and $dt = \frac{10^{-4}}{3}$. (*d*) Average number of visits for particles starting in the DL. Here, $N = 10^3$, $dt = \frac{10^{-4}}{3}$ (*circles*), and $\frac{10^{-6}}{3}$ (*diamonds*). The x axis is the same in all four plots; the plots are aligned. The shading guides the eye to the crossover region.

The plus symbols are simulation results. In simulations, the MFPT in this region will be limited by the simulation time; this is manifested in the saturation at MFPT $= 500$, since this was the simulation time. For simulation time $<1/s$, particles with initial condition in the AL will never enter the DL and therefore will not escape. The solid curves are $1/\sigma_1$ from the theoretical calculation, as explained in the section Analytical approach in the general case. Panel (a) displays an excellent match between theory and simulation. The MFPT for particles placed initially on the AL is limited by the time to transition to the DL at low s, which is why MFPT behaves as $1/s$ in this low s tail.

For s above ≈ 10, MFPT becomes insensitive to the initial layer (AL or DL), as can be seen by the identical simulation results in panels (a) and (b) in this range of s (the theory curves are identical in both panels). Thus, we now switch to discussing panel (b), and phenomenology for $s \gtrsim 10$ will be covered in that discussion.

For s below a value of ≈ 10, there is a horizontal plateau in panel (b). As s increases, the probability of visiting the AL also increases. Although the fraction of particles visiting the AL grows as $\propto s$, the time to remain in the AL (the longest timescale in this range of s) decreases as $\propto 1/s$, resulting in the plateau of MFPT versus s. Because the probability (or fraction) of visits to the AL is less than 1 (for particles starting in the DL), a particle has a chance to escape purely diffusively for s in this plateau region. The value of the MFPT in this plateau is discussed in Supporting Material E.

The probability of visiting the AL (for particles starting in the DL) eventually reaches 1 at larger s (see panel (c)). For these s values, particles are certain to visit the AL at least once; the probability of a purely diffusive escape is now zero. This happens when the diffusive time is comparable to the average switching time ($= 1/s$) and corresponds to $s \approx 10$, since the diffusive time is close to 0.1. For any s greater than this, each particle experiences intermittent advection, punctuated by periods of diffusion. In other words, on a typical run from an initial location to one of the boundaries, a particle's trajectory will include multiple episodes of advection and diffusion after each other. A cargo-motor complex diffuses in the cytoplasm, attaches to the MT, advects for some time, detaches back into the cytoplasm, diffuses, then attaches again, and so on. The number of such attachment events grows with s, as demonstrated in panel (d). As a result, the role of advection that brings particles back into the interior grows with s. As the propensity of particles to be thrown back into the interior grows, so does MFPT—for $v > 1$.

The situation for $s > 10$ is different if $v < 1$. A typical time spent in each layer is 0.1 or less. Thus, the distance advected over this time period is less than 0.1 if $v < 1$. In other words, the advective distance becomes less than the diffusive distance, so advection does not disturb the position of the particle while it spends time in the AL before switching back to the

DL. For this reason, MFPT is not affected by the increasing switching rate, and it does not rise if $v < 1$.

Going back to the $v > 1$ case, at sufficiently large switching rate, the second plateau is reached. Here the switching between the layers is so rapid that there's an effectively one-layer regime. This regime will be studied in Section one-layer limit. Interestingly, it is in this one-layer regime, where the dependence of MFPT on velocity is most pronounced, and this dependence scales exponentially in v. In contrast, velocity has essentially no effect on the MFPT for $s < 10$.

Because the region of s over which MFPT rises (if $v > 1$) connects two plateau regimes, we will call it the "crossover region"; i.e., it's a region in which the behavior crosses over from the one dominated by diffusion to the one where diffusion and advection play equal roles. This crossover region is broad—it can be several decades wide—and is marked by a drastic growth of the MFPT, especially at larger v. We indicate it in Fig. 4 by a shaded band. The location of the crossover—defined, for example, by the point of inflection—scales like v^4, as explained in Supporting Material H.

We comment in passing on the slight bump in the MFPT seen in Fig. 4 b—from the value of $\approx$ 0.1 to $\approx$ 0.2 at $s \approx 10^{-2}$. As suggested by the plot of the fraction of visits to the AL, at this switching rate, the fraction of simulation runs (out of N) that visited the AL becomes nonzero; below this crossover, the AL is not visited by any of N simulations, and the MFPT is a purely diffusive time $= 0.125$ (or 12.5 s using the example parameters of $L = 1$ μm and $= 10^{-2}$ $\mu m^2/s$). The absence of visits to the AL below a certain s is an artifact of the finite N. Despite a decreasing probability of visiting the AL with smaller s, increasing N would cause some simulations to reach the AL for s below 10^{-2}, and this bump in the MFPT would be pushed to smaller s. With an infinite number of simulations, the plateau with MFPT ≈ 0.2 would extend down to arbitrarily small s.

The story conveyed by Fig. 4 can be summarized as follows. Cargo that are produced close enough to MTs that they have a high likelihood of binding to one can be considered as starting in the AL. For such cargo, the MFPT shows an interesting nonmonotonic behavior. The values of MFPT at low switching rates are limited by the time to switch to DL. As the switching rate increases, the MFPT drops in proportion to $1/s$ as cargo can access the DL more and are able to escape quicker. However, when the switching rate becomes large enough that diffusive and switching times are comparable, more than one visit to both layers becomes likely, and we enter the intermittent regime where the MFPT increases and then saturates. For cargo initially produced off MTs, on the other hand, escape time (or MFPT) will be diffusive until the average switching time becomes comparable to the diffusive time. For switching times less than that, advection becomes significant, and the impact of advection increases with decreasing switching time, leading to an increase in MFPT. It eventually plateaus, or reaches a maximal value, as the cargo-motor complex experiences advection and diffusion equally. Here, the switching between AL and DL is so rapid that it is well-described by an effective one-layer model. In this regime, the MFPT depends most sensitively on v, and this dependence is exponential.

Supporting Material C displays examples of particle trajectories for a broad range of s that cover all of the behavioral regimes shown in Fig. 4. These figures demonstrate the change in the character of trajectories—from the types that contain advective periods long enough to arrive to the attractor at low s, to intermittent behavior in the crossover region, to very rapid switching between layers for s beyond the crossover—when the model is effectively in the one-layer regime.

So far, we presented results with $a = b$. If $a \neq b$, but the ratio a/b is fixed (for example, $b = 0.5a$ or $b = 2a$), the shapes of the MFPT curves will be qualitatively the same. As one would expect, if $b/a < 1$ (for example, $b = 0.5a$), the MFPT would be larger than if $a = b$—since particles spend more time in the AL, suppressing escape. Conversely, if $b/a > 1$ (for example, $b = 2a$), MFPT is smaller than if $a = b$—since particles spend more time in the DL, promoting escape.

Quantitative connections to intracellular transport

We first make the general observation that the crossover (where MFPT increases dramatically) takes place between $s = 10$ and $s = 10^4$. Remarkably, this is the general range of these parameters found in cells; see "range of parameters" in the materials and methods section. This suggests that cells are able to exploit the full dynamical range of behaviors. Indeed, the crossover region is where a change in parameter (the on-/off-rate) gives rise to the largest change in the outcome (MFPT)—especially at larger values of v. Thus, cells can exploit the entire range of transport modalities, from trapping to dispersal, for a single cargo by regulating the parameter values or simultaneously exploiting different modalities for different cargos with different intrinsic parameters.

We now relate our theoretical predictions quantitatively to the specific biological example of transport in the quasi-one-dimensional geometries of axons and dendrites. To do so, we first estimate the actual values of our model parameters for this system. Velocities of $0.6 - 2$ $\mu m/s$ for 30- to 40-nm-sized vesicles were reported (37) in axons of *C. elegans*. Similar

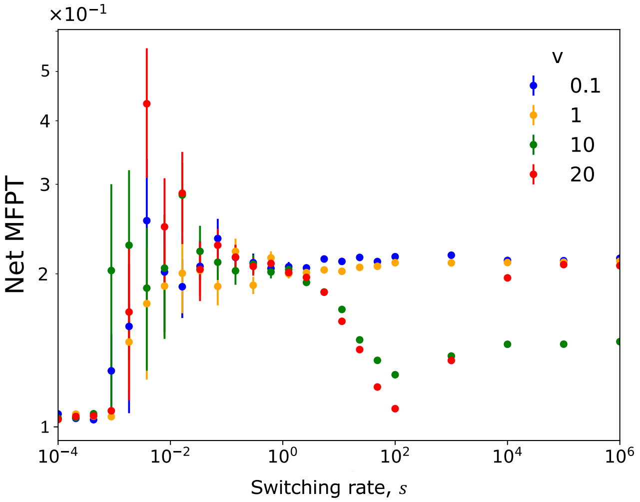

FIGURE 5 Simulation results for asymmetric case: $X = 0.85$. In this particular case, $x_0 = 0.7$, but such dips are also present at other x_0. The initial condition is on the DL. Errors bars represent the standard error of mean.

speeds have been reported for motor-driven transport of mitochondria—a much larger organelle—in axons and dendrites (38), (39) as well as for the motor-driven velocities of peroxisome vesicles in dendrites of hippocampal neurons (40). Thus, the advective velocities of motors on MTs in axons and dendrites can be taken to be of the order of 1 $\mu m/s$. On- and off-rates on the order of 0.1 s^{-1} have been estimated and reported (41),(35), (42) for different axonal and dendritic cargo. Cytoplasmic diffusion coefficients for small vesicles in neurons have been reported to be in the range of 0.025 $\mu m^2/s$ to ≈ 0.06 $\mu m^2/s$ depending on crowding conditions (43).

Based on these literature values, we will use the value 1 $\mu m/s$ for advective speed, $0.1 - 1$ s^{-1} for on- and off-rates, $0.01 - 1$ $\mu m^2/s$ for diffusion coefficient, and $1 - 10$ μm as a range of MT lengths that we reported in the "range of parameters" section. This gives the following range of dimensionless parameters: $1 < v < 10^3$, $10^{-1} < s < 10^4$. Note that this range of s covers the crossover region—where MFPT increases dramatically by many orders of magnitude. Although the range of s alone is too wide to call this behavior "sensitive dependence of MFPT upon a change in s," including an additional freedom in adjusting dimensionless advective velocity justifies this term, because MFPT scales exponentially with v in the second plateau (see "one-layer limit" section). Consider, for example, $s = 300$ and $v = 20$, which according to our $1/\sigma_1$ theory gives $\tau \approx 3.1$ (if $D = 0.1$ $\mu m^2/s$ and $L = 5$ μm, then dimensionless $v = 20$ corresponds to a physical velocity of 0.4 $\mu m/s$ and $s = 300$ corresponds to switching rate of 1.2 s^{-1}—all very realistic; then $\tau = 3.1$ corresponds to ≈ 13 minutes). Increasing s by a factor of 2 (for example, by increasing the on and off-rate by this factor) gives $\tau \approx 7.6$. However, if we now also increase v by a factor of 2, we get $\tau \approx 34$. On the other hand, $s = 300$ and $v = 40$ would have given $\tau \approx 6.7$ Thus, realistic changes of multiple parameters together, which could happen for different cargos carried by different motors on the same filaments, resulted in an overall increase of MFTP by an order of magnitude.

Our findings suggest that the occurrence of neighboring MTs that face each other with the opposite polarity can have a strong effect on slowing down transport of cargo down the length of dendrites—and the propensity for this changes most rapidly in the crossover region.

Asymmetric attractor placement results in an optimal on-/off-rate that minimizes the MFPT

We now consider the effect of asymmetric attractor placement; i.e., the attractor is closer to one end of the domain (exit) than the other. We found that placing the attractor asymmetrically can give rise to a counterintuitive decrease in MFPT with increasing switching rate; see $1 < s < 10^2$ in Fig. 5 (the rise in MFPT at $s \approx 10^{-2}$ is due to the finite N effect described above). This effect is only seen at larger v (contrast the behaviors of $v = 0.1, 1$ versus $v = 10, 20$). The decrease happens over a range of $1/s$ that is comparable to the advective time, $\sim 1/v$. For example, for $v = 20$, the timescale to travel advectively to the attractor is ~ 0.05, whereas the decrease is seen for s between 1 and 100, which corresponds to the timescale between 1 and 0.01.

We can explain this dip as follows. At sufficiently large switching rate (≈ 1 in Fig. 5), the escape through the end far from the attractor becomes unlikely, and most of the particles exit through the close end, lowering the MFPT.

Further increase of s causes all escape events to be rare, and particles congregate around the attractor for a long time, leading to another increase in the MFPT (we see that at $s \approx 10^2$ in Fig. 5). Additional discussion to support this explanation can be found in Supporting Material G.

Fig. 6 shows an example of the dip phenomenon due to only the parameter a varied at fixed b. The dips in Fig. 6 happen again for asymmetric attractor placement, because increasing a causes particles to return back to the attractor, thus minimizing the chance for them to wander too far while diffusively exploring the long part of the domain. On the other hand, increasing a even further tends to keep the particles in the AL and therefore prevents them from escaping (particles cannot move in the direction of

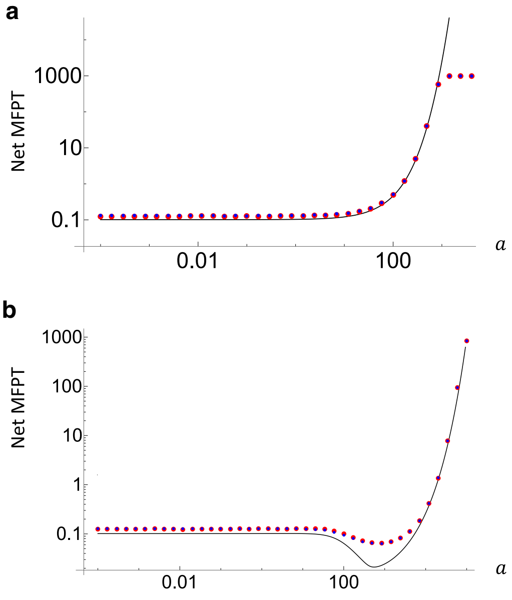

FIGURE 6 $\tau(a)$ at fixed $b = 169$. (*a*) $X = 0.5$, and (*b*) $X = 1/26$. $v = 13$ for both. Lines, theory; dots, simulation. Red dots, IC on the diffusive layer; blue dots, IC on the advective layer. The numbers for the two types of initial conditions are not identical, but the difference is almost invisible. The theory prediction is $1/\sigma_1$, the inverse of the ground state eigenvalue, which is an approximation of the exact MFPT. The IC in the simulation was at $x_0 = 0.5$. The simulation time was 1000, which is the reason for flattening of the simulation data at large *a* in (*a*).

the ends when they are in the AL due to the advective flow being directed toward the attractor).

These dips are somewhat counterintuitive—an overall escape time is lowered by increasing the tendency to go toward the attractor inside the domain—as long as the attractor is placed asymmetrically. A similar phenomenon has been reported in connection to the problem of MFPT with a reset (24), (25), (44). Here, in addition to diffusion, a particle experiences a reset back to some location, and resets form a Poisson process, endowed with a reset rate *r*. The authors found there exists an optimal rate, r^*, which minimizes the MFPT out of the semiinfinite domain. We note, however, that these studies return the particle back to the reset location once it has hit the absorbing end of the semiinfinite domain, thereby conserving the probability. This is different from our problem, in which the total probability inside the domain decreases with time, because once particles have reached one of the two absorbing ends, they are not returned back into the domain.

This difference aside, the problem that we are analyzing can be viewed as a version of a reset problem, although the time to reset is not instantaneous. Moreover, the reset location is not necessarily the location of the attractor $x = X$, since a particle has a chance to return to the DL before reaching the attractor.

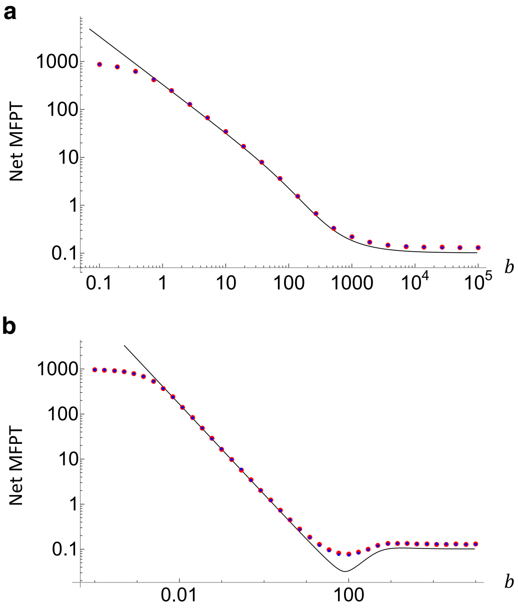

FIGURE 7 $\tau(b)$ at fixed $a = 169$. (*a*) $X = 0.5$, and (*b*) $X = 1/26$. $v = 13$ for both. Lines, theory; dots, simulation. Red dots, IC on the diffusive layer; blue dots, IC on the advective layer. The theory prediction is $1/\sigma_1$, the inverse of the ground state eigenvalue, which is an approximation of the exact MFPT. The IC in the simulation was at $x_0 = 0.5$. We again see saturation of simulation results at low *b* at the simulation time (here, 1000 time units).

The limit of infinite *v* would correspond to the instantaneous reset to the attractor, and the limit $b \to 0$ would cause the resetting to take particles back to $x = X$, i.e., approximating the standard reset problem (although, again, without returning of particles that have reached either of the domain ends).

The dip phenomenon is also observed when *b* is varied at fixed *a*; see Fig. 7. At low *b*, MFPT is dominated by the waiting time $1/b$ to return from the attractor to the DL. A large *b* asymptote (for $b \gg a$) is the regime of purely diffusive motion; the particles are forced into the DL. Evidently, having some acccess to the AL leads to a lowering of MFPT because it allows more material to congregate close to one end.

It is interesting to ask what effect increasing the advective velocity would have. The intuition—supported by the physics of the one-layer model—is that higher *v* should lead to either an increase of the MFPT or the disappearance of the dip, because with sufficiently large velocity, the density will be more and more localized near the attractor; so, even though the attractor is closer to one end than the other, it is no longer close to this end in comparison to the width of the density distribution. However, analytical calculations in fact predict the decrease in the value of $1/\sigma_1$ at a fixed *a* with increasing *v*; see Fig. 8.

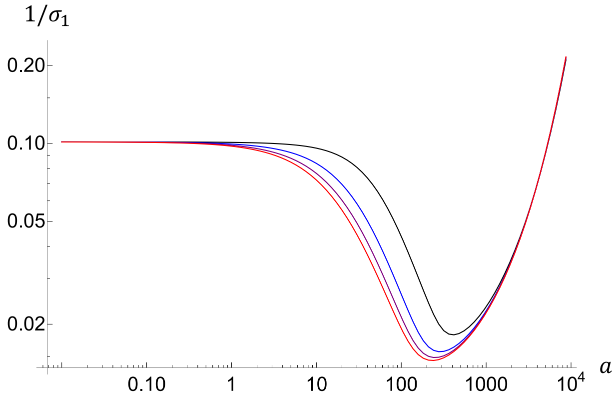

FIGURE 8 Top to bottom: $v = 20$ (*black*), 40 (*blue*), 60 (*purple*), and 80 (*red*). Here, $X = 1/26$, and $b = 169$.

Fig. 9S (in Supporting Material F) sheds light on the reason for this counterintuitive prediction. Although the density profile in both layers does become more localized with larger velocity (as expected), the part of the profile between the attractor and the close end is not affected; the decrease in the spread is due to the other side of the profile. Therefore, as velocity is increased, more and more material is localized near the close end, whereas the chance of escaping through this end does not diminish—resulting in the overall decrease of escape time.

We also study the effect of varying X in Fig. 9. Here the results conform to the intuitive expectation that a decrease in asymmetry will lead to a decrease in the magnitude of the dip (with no dip at all in a completely symmetric geometry). An attractor placed much closer to the left end than the right one prevents particles from wandering too far to the right (by increasing a, and thus the reset rate), causing the particles to congregate closer to the left end in the more asymmetric situation, thus leading to a lower MFPT.

The existence of such an optimum in escape times as a function of on-/off-rates that is additionally tunable by velocity is an interesting feature that cells could potentially exploit. Firstly, they can achieve faster than diffusion export using a naturally occurring MTOC stabilized MT geometry and dynein motors that walk toward the MTOC. Secondly, this export can be spatially directed to a location close to the MTOC (which is not possible with motors that walk away from the MTOC). Such directed export using an MTOC and dynein-transported cargo occurs in the export of lytic granules from immune cells (22,23). Lytic granules aggregate at the MTOC, which is positioned near the immunological synapse, directing the export of toxic granules to the target cell. In fact, in this case, cells exploit both aggregation due to symmetric MTOC positioning as well as more effective dispersal due to asymmetric positioning that accelerates site-directed export by moving the MTOC close to the synapse.

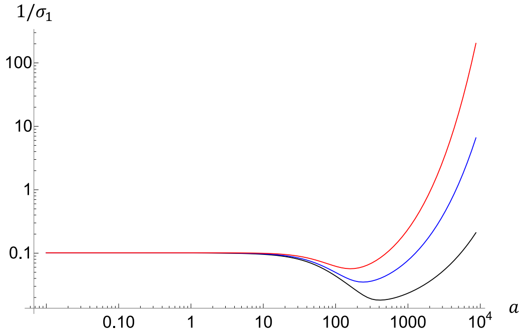

FIGURE 9 Top to bottom: $X = 3/26$ (*red*), $2/26$ (*blue*), and $1/26$ (*black*). Here, $v = 20$, and $b = 169$.

One-layer limit

Dynamics of probability density

In our discussion of Fig. 4, we mentioned that for sufficiently large rate of switching between layers, the system reduces to an effectively one-layer model. Remarkably, it is in this one-layer regime where the dependence on velocity is most pronounced. In the purely diffusive escape, advection is not felt, and variation of v has no effect. As the probability to reach the AL is increased, the effectiveness of the advection grows. The system experiences advection for part of the time, and variation of v will have some effect; we see this in the crossover region. In the one-layer limit (at sufficiently large s), the system experiences advection continuously, and MFPT is most sensitive to variations of v; we see this in the second plateau region. For sufficiently large v, escape is a rare event, and MFPT scales exponentially with v.

The one-layer situation is similar to activated dynamics of a particle in a potential energy well (45). The random kicking by stochastic forces (which are represented by diffusion in the equation for the evolution of probability) has a tendency to kick the particle out of the well, whereas the force from the well pulls the system back toward the attractor. A competition between these two effects will give rise to an exponential dependence of MFPT. Here, we examine this process in detail.

The analytical approach in the one-layer limit is outlined in the materials and methods section, with details in Supporting Material B. These predictions are verified by simulations (see Supporting Material D). Here, we present results of analytical calculations.

We show in Fig. 10 several snapshots in the evolution of the probability density profiles for a specific

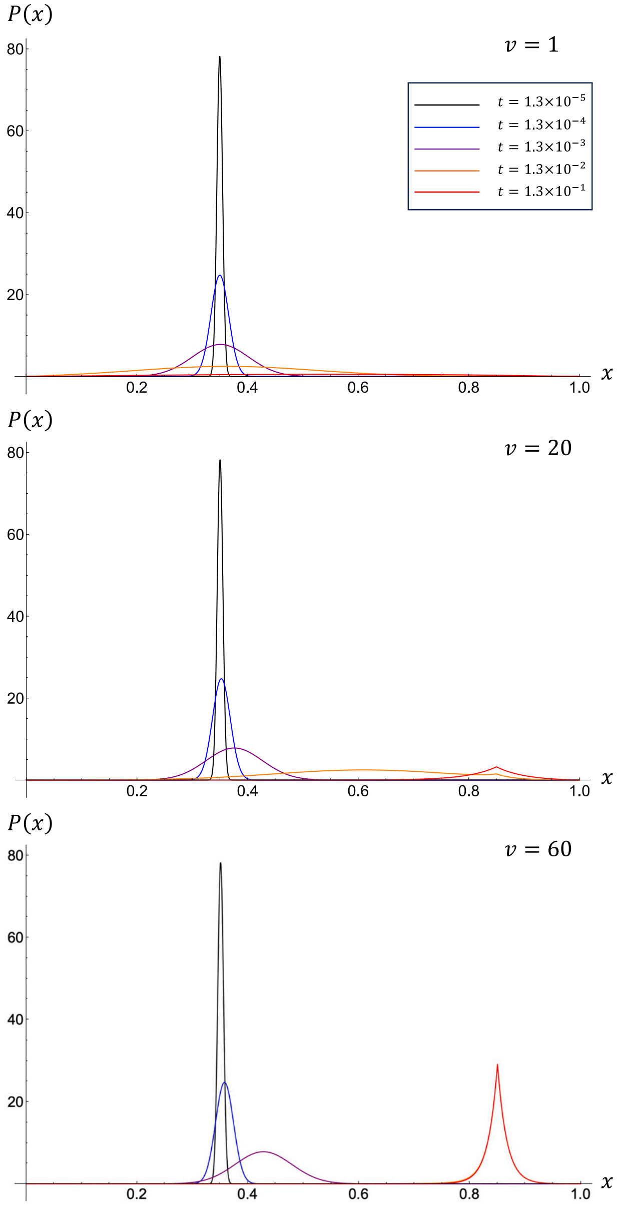

FIGURE 10 $X = 0.85$, and $x_0 = 0.35$. The distributions are shown for $t = 1.3 \times 10^{-5}$ (*black*), $t = 1.3 \times 10^{-4}$ (*blue*), $t = 1.3 \times 10^{-3}$ (*purple*), $t = 1.3 \times 10^{-2}$ (*orange*), and $t = 1.3 \times 10^{-1}$ (*red*). Top, $v = 1$; middle, $v = 20$; bottom, $v = 60$. For $v = 1$, the distributions never reach an asymptotic form that is centered on $x_0 = X$. For $v = 60$, the profiles at $t = 1.3 \times 10^{-2}$ and at $t = 1.3\times 10^{-1}$ are almost the same.

placement of the attractor and specific initial condition, for three values of the advective velocity. Following a δ-function initial condition, there is a quick diffusive spread. Although this spread is happening, the center of the distribution is also advected toward the attractor.

At $v = 20$, we begin to see the emergence of a large-time asymptotic profile centered on the attractor; the distribution reaches a stationary limiting form. For example, for $v = 20$, the width stops evolving at $t \approx 0.06$, and the cusp-shaped profile is established in the vicinity of the attractor. As this limiting profile develops, the diffusive spread of the density profile is followed by a contraction, as particles congregate around the attractor and σ_x decreases. After the limiting form has been established, the probability to remain in the domain continues to decrease (the area under the curve will continue to decrease) as particles exit, although the shape of the profile remains stationary. For $v = 20$, the cusp profile at the time shown contains visibly less area under it than at earlier times; some of it was lost before this profile formed (and the profile itself continues to lose area at a noticeable rate at future times over similar timescales). However, in the case of $v = 60$, there's hardly any area loss before the formation of the limiting profile (and the profile itself will not show any noticeable area loss at future times over similar timescales). In the $v = 1$ case, the particles escape before any profile centered on the attractor has time to establish; the profile evolution is similar to the evolution in the absence of any advection. For example, the average position of particles reaches $1/2$ in the $v = 1$ case. On the other hand, at $v = 20$ and $v = 60$, the center of the distribution reaches the attractor at $x = X$.

All in all, the picture is this: the attractor captures some particles and pulls them into its vicinity at larger v, whereas at lower v, most of the particles escape before this happens. The decay rate also decreases; as v grows ever larger, the large-time limiting profile localized around the attractor will decay ever slower, its rate of decay decreasing exponentially with v (this is for sufficiently large v; i.e., it is an asymptotic scaling). In this large v regime, the profile that develops after an initial rapid relaxation may be called quasistationary—as it decays on a timescale much larger than all other timescales in the problem. This is the regime of rare events, and we now discuss the scaling of MFPT and escape probabilities in this limiting regime.

Scaling of MFPT in the rare event limit

In this regime, various functions of x_0—such as the escape probability and escape time—develop characteristic distinctions between a boundary layer and interior regions. This is shown in Fig. 11. As v increases, the MFPT to exit increases, and eventually, this time becomes much larger than all the other characteristic timescales of the problem. In this large v regime, escape becomes a rare event. Starting from an initial condition x_0, a particle will, with overwhelming probability, drift toward the attractor and fluctuate around it for a time that scales exponentially

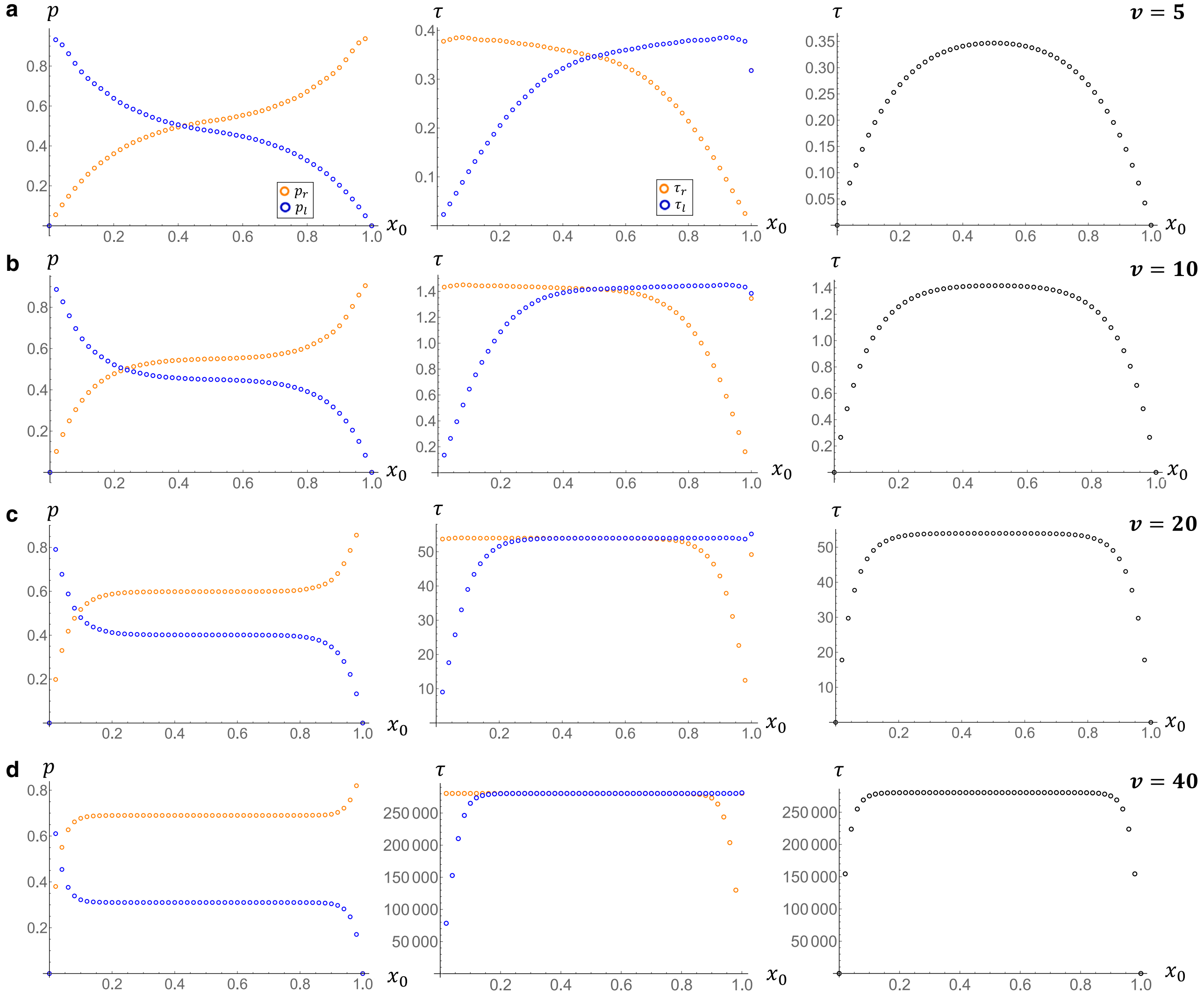

FIGURE 11 Escape probability and MFPT through both ends versus the location x_0 of the IC. The attractor is located at $X = 0.51$. (*a*) $v = 5$, (*b*) $v = 10$, (*c*) $v = 20$, and (*d*) $v = 40$. The aberrations at the edge are numerical artifacts.

with v. Therefore, the initial condition will be forgotten long before it exits the domain. This effect is manifested in Fig. 11 by distinct plateaus that show the absence of dependence on x_0. We show the comparison between such analytical predictions and simulation results of the one-layer regime in Supporting Material D.

The velocity field is minus the derivative of the following potential: $U(x) = v(X - x)$ for $0 < x < X$ and $U(x) = v(x - X)$ for $X < x < 1$. Thus, the effective activation barrier to escape from the attractor to the left end of the domain is $\Delta U_l = vX$, whereas the effective barrier to escape to the right end is $\Delta U_r = v(1 - X)$. On the timescale much smaller than the MFPT, the probability current through the left end will be $j_l \sim e^{-\Delta U_l}$, and the current through the right end will be $j_r \sim e^{-\Delta U_r}$ (we're only focusing on factors that are exponential in v, hence the $\sim$). The net current is $j \sim e^{-vX} + e^{-v(1-X)}$. Therefore, the net MFPT is $\tau \sim \left(e^{-vX} + e^{-v(1-X)}\right)^{-1}$. However, due to the exponential scaling with v, only one of these terms will be dominant. For $0.5 < X < 1$, it will be $\tau \sim e^{v(1-X)}$, and for $0 < X < 0.5$, $\tau \sim e^{vX}$. In both cases, we get the exponential scaling of the MFPT seen in the right-hand panel of Fig. 11.

One comment regarding MFPT results is in order. We notice that the overall MFPT τ in Fig. 11 is about two times smaller than the $a = b \rightarrow \infty$ limit in Fig. 4 (see $v = 10$ and $v = 20$ graphs). Although a small difference is due to slightly different X (0.51 in Fig. 11 versus 0.5 in Fig. 4), the main reason for this difference is that in the two-layer problem, the advection and diffusion take turns, whereas they take place simultaneously in the two-layer model. Thus, all

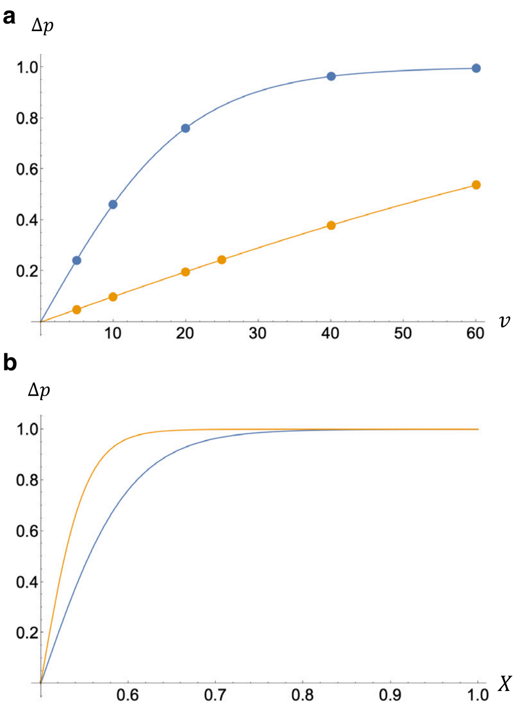

FIGURE 12 Difference in escape probability Δp vs. parameters. (*a*) Δp versus v. Top (*blue*), $X = 0.55$; bottom (*orange*), $X = 0.51$. Dots, full theory; solid curves, Eq. (15). (*b*) Δp vs. X, given by Eq. (15). Top (*orange*), $v = 20$; bottom (*blue*), $v = 10$.

timescales are slowed down by exactly a factor of 2 in the two-layer model versus its truly one-layer equivalent. In other words, to make the proper comparison, we must multiply the one-layer MFPT by 2 to match the $a = b \to \infty$ limit of the two-layer model.

Small asymmetry leads to a large bias in the exit location

One prominent feature of Fig. 11 is the amplification in the asymmetry in results (for example p_l and p_r—probabilities to escape through the left and right ends, respectively) due to a small asymmetry in the placement of the attractor. Note that $p_r = ae^{-\Delta U_r}$ and $p_l = ae^{-\Delta U_l}$, where a is some constant. We can find this constant from the fact that $p_r + p_l = 1$ (a particle definitely exists through one of the two ends eventually). Thus, $a = (e^{-\Delta U_r} + e^{-\Delta U_l})^{-1}$, altogether giving

$$\Delta p \equiv p_r - p_l = \tanh[(X - 1/2)v] \qquad (15)$$

We overlay this prediction on top of Δp obtained from the analytic results (depicted in Fig. 11) in Fig. 12 *a*.

Note that whereas there's a growing difference between p_l and p_r due to asymmetry, MFPTs to escape through each end are the same in the plateau region. The τs in the middle column of Fig. 11 are MFPTs conditioned on the exit location. Thus, a system is much more likely to escape from the closer end when v is sufficiently large, but those few systems that do manage to escape from the further end will escape in essentially the same amount of time.

It is interesting to consider that cells could potentially exploit the exponential sensitivity of exit location to attractor placement in this regime of parameters. Thus, cells with noncentrosomal MTOCs that are located off-center could guarantee export to the closest adsorbing boundary (either cellular or organelle membrane), albeit at the expense of a very long transport time. Centrosomal MTOCs that are close to being symmetrically positioned sit at a critical point. Slight relocations toward an adsorbing boundary could also create a dominant preference for cargos to end up at some defined region of the cell periphery or organelle in that direction.

DISCUSSION

In this article, we looked at a one-dimensional model of intracellular transport via a combination of advection on MTs and diffusion in the cytoplasm. This one-dimensional model was primarily motivated by a scenario involving an attractor in the interior of the cell—for example, the MTOC. There are, however, other situations where attractors may arise. Consider the β cell example from the introduction. Here, motors transport insulin granules along MTs. Due to orientational disorder (46), several MTs can meet with ends of the same polarity facing each other, forming an aster-like morphological trap (or attractor) for motors that would all congregate at this junction (11). It is meaningful to talk about the domain of attraction of such a trap in the following sense. A molecular motor that attaches to an MT anywhere within this domain will be taken toward the attractor, whereas a motor that attaches to an MT outside of the domain has a chance to follow an MT that leads away from a trap. When placed inside such a domain—where advective motion along MTs tends to only attract particles—they can nevertheless escape the domain of attraction of the attractor by desorbing from MTs and diffusing within the cytoplasm until they end up outside of the domain. Naturally, a question about the time to be stuck in the vicinity of the attractor arises—along with the question of how formation of such traps affects the functioning of the cell and the overall transport of insulin granules across it.

Using our one-dimensional model, we calculated the escape probability for cargo through each end of the domain, the MFPT to escape the domain through each end, and the overall escape probability and MFPT as a function of the following: the initial location of the cargo (site of production in the cell), the location of the attractor (MTOC) toward which the advective motion is directed, the advective velocity v, and the cargo on-/off-rates.

We made several predictions. When the attractor is placed symmetrically, there is a crossover in switching rates s causing the MFPT to change from $\tau \sim 0.1$ (diffusive timescale) to τ that grows exponentially in v. The range of s over which this crossover happens is wide—several orders of magnitude—but it corresponds to switching rates actually found in cells. This served as our first example of tunability that allows cells to achieve large changes in the functionality by changing regulatory parameters or even simultaneously exploiting different transport modalities (trapping or dispersal) for different cargos with different intrinsic parameters being transported on the same cytoskeletal architecture.

For s significantly below the crossover, a particle that was released into the DL has a chance to escape the domain purely diffusively without ever visiting the AL. For s at the low end of the crossover region, the probability of this goes to zero; every particle will be advected toward the attractor for at least some of the time. For s above the high end of the crossover region, the transport enters an effective one-layer regime and exhibits rare event physics.

Asymmetric placement of the attractor gives rise to an interesting phenomenon of an optimal switching rate or an optimal on- or off-rate individually. Thus, we found that it is possible to minimize the residence time in the domain by increasing the on- or off-rate, because that will lower the diffusive spread and bring particles close to one end of the domain. It is interesting to speculate whether the parameter rates for cargos that need to be dispersed (while simultaneously sequestering other cargo) could be tuned to this optimal regime and whether it is, in fact, being exploited by cells like the immune cells to export lytic granules.

We discussed the effective one-layer regime that results at sufficiently large on-/off-rate. We also discussed the rare event physics that happens at large dimensionless advective velocities. In such a rare event regime, a portion of particles will be localized in the vicinity of the attractor for a time exponentially long in v. We provide an explicit form of this exponential dependence v.

The idea of exponential sensitivity and phenomena such as strong amplification of the preferred exit end due to a slight asymmetry is tantalizing. Extrapolating this finding to two dimensions suggests that in complex, crowded environments that allow for multiple trap-like morphologies (for example, asters), the distribution of cargo around the cell will be nonhomogeneous. This remains to be verified in the future, by extending our model to two dimensions. It is also interesting to speculate whether cells could benefit functionally from guaranteeing high specificity of export location at the expense of long transport times, in which case the exponential sensitivity we have shown could be very useful.

Our analysis is one-dimensional. Throughout the article, we used dendrites as an example in which such analysis would be applicable. Yet, the majority of converging MT morphologies take place in two and three dimensions. Such work is underway. In the meantime, we cautiously anticipate that the following aspects of our one-dimensional findings would translate to higher dimensions. First, consider the crossover in Fig. 4 in which MFPT can experience a dramatic growth by many orders of magnitude. This happens when cargos are prevented from a purely diffusive escape; the crossover begins where the probability of visiting the AL becomes 1. With sufficiently large on-rates, this this is guaranteed to happen, and if v is greater than 1, we witness the MFPT increase. In two dimensions with radial MT morphologies, taking the on-rate arbitrarily large will not prevent some of the particles from escaping diffusively. Therefore, we expect that a dramatic rise in MFPT will only happen with initial conditions sufficiently close to the convergence point. The more MTs there are, the larger is this region of initial conditions that will result in the strong increase of MFPT. A similar comment can be made concerning the rare event behavior. For initial conditions not in this region that guarantee a high chance of hitting MTs (i.e., close to the convergence point), a majority of cargos will escape the cell (or the domain of attraction of the convergence point) by purely diffusive mechanism. The remaining particles will be trapped at the MTOC for a time that scales exponentially in v.

We also expect the reasoning for the optimal off-rate seen in Fig. 7 to remain in two dimensions. Forcing cargo off of MTs will result in purely diffusive times, but allowing particles to remain on MTs will result in a greater accumulation at the MTOC—which if placed asymmetrically will lower the overall MFPT.

Our work contributes a new perspective from a purely mathematical perspective as well. The modeling approach that we use involving two density variables—one governed by advection and the other by diffusion—is not new. For example, this framework has been employed by (35) or by (47). However, neither paper is concerned with the questions that we pose—the effectiveness of MTOCs in trapping cargo. Neither work is framed as a problem of escape, calculation of MFPTs, escape probabilities, or trapping probabilities. The work by (47) concerns the situation of constant v—a situation that allows traveling waves.

The authors discuss these traveling wave solutions. On the other hand, (35) is interested in unidirectional and bidirectional transport in axons and dendrites. The authors do study spread (or dispersion) of particles throughout the domain, and they also calculate currents. However, they are not interested in the question of MFPTs; that is, their advective field doesn't have an attractor, and they also use different boundary conditions. On the other hand, when we use our model in the context of a dendrite, the domain of length L is not the whole dendrite but only the length of two MTs that face each other with opposite polarity. Here the MFPT is a measure of the residence time in the trap created by this local MT arrangement. The review by Bressloff (48) also mentions models of similar type. Here, they describe a particle in three possible states; it can advect to the right, to the left, or it can diffuse. This is described by three coupled equations—two advective and one diffusive. Our work is complementary to other prior theoretical models of transport that involve a combination of diffusion and advection along MTs—for example, (49) and (50). However, here too, neither of these sources are focusing on questions of residence time or the role of asymmetry.

Interesting extensions to our work could include studying models with reflecting-reflecting or absorbing-reflecting boundary conditions or models in which the source is on one end and the target is on the other. Such models would be better suited for transport of cargo in cilia (4), transport between the plasma membrane and Golgi apparatus (5), (6), or between endoplasmic reticulum and Golgi (7), (3), transport of viruses toward replication sites (8), (9), and other intracellular transport situations (3), (10).

DATA AND CODE AVAILABILITY

The data and code that support the findings of this paper are available upon reasonable request from the authors.

SUPPORTING MATERIAL

Supporting Material can be found online at https://doi.org/10.1016/j.bpr.2024.100171.

AUTHOR CONTRIBUTIONS

N.S. performed simulations and contributed to writing the paper, B.R. helped with analytical calculations, A.G. conceptualized the project and contributed to writing the paper, and O.K. performed analytical calculations and contributed to writing the paper. N.S., A.G., and O.K. all contributed to framing questions, formulating calculations or simulations that needed to be performed, and analyzing the results.

ACKNOWLEDGMENTS

This work was supported by the National Science Foundation (NSF-DMS-1616926 to A.G.) and NSF-CREST: Center for Cellular and Biomolecular Machines at UC Merced (NSF-HRD-1547848 and 2112675 to A.G.). A.G. and N.S. also acknowledge partial support from the NSF Center for Engineering Mechanobiology grant CMMI-154857 and computing time on the Multi-Environment Computer for Exploration and Discovery (MERCED) cluster at UC Merced (NSF-ACI-1429783). N.S. acknowledges Graduate Student Opportunity Program Fellowship from the University of California, Merced. B.R. and O.K. acknowledge that this research was generously supported by the William and Linda Frost Fund in the Cal Poly Bailey College of Science and Mathematics.

N.S. was at University of California, Merced, for part of the project, B.R. was at California Polytechnic State University (Cal Poly), San Luis Obispo, while she was working on the project, and O.K. was also at Cal Poly, San Luis Obispo, for part of the project.

DECLARATION OF INTERESTS

The authors declare no competing interests.

REFERENCES

1. Howard, J., and R. Clark. 2002. Mechanics of motor proteins and the cytoskeleton. *Appl. Mech. Rev.* 55:B39.
2. Ross, J. L., M. Y. Ali, and D. M. Warshaw. 2008. Cargo transport: molecular motors navigate a complex cytoskeleton. *Curr. Opin. Cell Biol.* 20:41–47.
3. Mogre, S. S., A. I. Brown, and E. F. Koslover. 2020. Getting around the cell: physical transport in the intracellular world. *Phys. Biol.* 17:061003.
4. Chien, A., S. M. Shih, …, A. Yildiz. 2017. Dynamics of the IFT machinery at the ciliary tip. *Elife.* 6:e28606.
5. Yadav, S., and A. D. Linstedt. 2011. Golgi positioning. *Cold Spring Harbor Perspect. Biol.* 3:a005322.
6. Mascanzoni, F., R. Iannitti, and A. Colanzi. 2022. Functional Coordination among the Golgi Complex, the Centrosome and the Microtubule Cytoskeleton during the Cell Cycle. *Cells.* 11:354.
7. Presley, J. F., N. B. Cole, …, J. Lippincott-Schwartz. 1997. ER-to-Golgi transport visualized in living cells. *Nature.* 389:81–85.
8. Greber, U. F., and M. Way. 2006. A superhighway to virus infection. *Cell.* 124:741–754.
9. Lagache, T., and D. Holcman. 2008. Quantifying intermittent transport in cell cytoplasm. *Phys. Rev.* 77:030901.
10. Valm, A. M., S. Cohen, …, J. Lippincott-Schwartz. 2017. Applying systems-level spectral imaging and analysis to reveal the organelle interactome. *Nature.* 546:162–167.
11. Ando, D., N. Korabel, …, A. Gopinathan. 2015. Cytoskeletal network morphology regulates intracellular transport dynamics. *Biophys. J.* 109:1574–1582.
12. Maelfeyt, B., S. A. Tabei, and A. Gopinathan. 2019. Anomalous intracellular transport phases depend on cytoskeletal network features. *Phys. Rev. E.* 99:062404.
13. Maelfeyt, B., and A. Gopinathan. 2019. Cytoskeletal filament length controlled dynamic sequestering of intracellular cargo. Preprint at arXiv. https://doi.org/10.48550/arXiv:1907.06329.
14. Hafner, A. E., and H. Rieger. 2018. Spatial cytoskeleton organization supports targeted intracellular transport. *Biophys. J.* 114:1420–1432.

15. Sallee, M. D., and J. L. Feldman. 2021. Microtubule organization across cell types and states. *Curr. Biol.* 31:R506–R511.
16. Oberhofer, A., E. Reithmann, ..., Z. Ökten. 2020. Molecular underpinnings of cytoskeletal cross-talk. *Proc. Natl. Acad. Sci. USA.* 117:3944–3952.
17. Bracey, K. M., K.-H. Ho, ..., W. R. Holmes. 2020. Microtubules regulate localization and availability of insulin granules in pancreatic beta cells. *Biophys. J.* 118:193–206.
18. Masucci, E. M., P. K. Relich, ..., E. L. Holzbaur. 2021. Kinesin-4 motor teams effectively navigate dendritic microtubule arrays through track switching and regulation of microtubule dynamics. Preprint at bioRxiv. https://doi.org/10.1101/2021.02.28.433181.
19. Sanchez, A. D., and J. L. Feldman. 2017. Microtubule-organizing centers: from the centrosome to non-centrosomal sites. *Curr. Opin. Cell Biol.* 44:93–101.
20. Masucci, E. M., P. K. Relich, ..., E. L. Holzbaur. 2022. Microtubule dynamics influence the retrograde biased motility of kinesin-4 motor teams in neuronal dendrites. *Mol. Biol. Cell.* 33:ar52.
21. Snider, J., F. Lin, ..., S. P. Gross. 2004. Intracellular actin-based transport: how far you go depends on how often you switch. *Proc. Natl. Acad. Sci. USA.* 101:13204–13209.
22. Nath, S., L. Christian, ..., M. Poenie. 2016. Dynein separately partners with NDE1 and dynactin to orchestrate T cell focused secretion. *J. Immunol.* 197:2090–2101.
23. Mentlik, A. N., K. B. Sanborn, ..., J. S. Orange. 2010. Rapid lytic granule convergence to the MTOC in natural killer cells is dependent on dynein but not cytolytic commitment. *Mol. Biol. Cell.* 21:2241–2256.
24. Evans, M. R., and S. N. Majumdar. 2011. Diffusion with stochastic resetting. *Phys. Rev. Lett.* 106:160601.
25. Evans, M. R., and S. N. Majumdar. 2011. Diffusion with optimal resetting. *J. Phys. Math. Theor.* 44:435001.
26. Stuart, G., N. Spruston, and M. Häusser. 2016. Dendrites. Oxford University Press.
27. Müller, M. J., S. Klumpp, and R. Lipowsky. 2008. Motility states of molecular motors engaged in a stochastic tug-of-war. *J. Stat. Phys.* 133:1059–1081.
28. Sarpangala, N., and A. Gopinathan. 2022. Cargo surface fluidity can reduce inter-motor mechanical interference, promote load-sharing and enhance processivity in teams of molecular motors. *PLoS Comput. Biol.* 18:e1010217.
29. Bovyn, M., B. R. Janakaloti Narayanareddy, ..., J. Allard. 2021. Diffusion of kinesin motors on cargo can enhance binding and run lengths during intracellular transport. *Mol. Biol. Cell.* 32:984–994.
30. Leduc, C., O. Campàs, ..., J. Prost. 2004. Cooperative extraction of membrane nanotubes by molecular motors. *Proc. Natl. Acad. Sci. USA.* 101:17096–17101.
31. Höög, J. L., C. Schwartz, ..., C. Antony. 2007. Organization of interphase microtubules in fission yeast analyzed by electron tomography. *Dev. Cell.* 12:349–361.
32. Melbinger, A., L. Reese, and E. Frey. 2012. Microtubule length regulation by molecular motors. *Phys. Rev. Lett.* 108:258104.
33. Xu, J., Z. Shu, ..., S. P. Gross. 2012. Tuning multiple motor travel via single motor velocity. *Traffic.* 13:1198–1205.
34. Schnitzer, M. J., K. Visscher, and S. M. Block. 2000. Force production by single kinesin motors. *Nat. Cell Biol.* 2:718–723.
35. Smith, D. A., and R. M. Simmons. 2001. Models of motor-assisted transport of intracellular particles. *Biophys. J.* 80:45–68.
36. Gardiner, C. W. 1985. Handbook of stochastic methods for Physics, Chemistry, and the Natural Sciences, 2nd ed. Springer series in Synergetics, Berlin.
37. Nair, A., S. Ramanarayanan, ..., M. Sivaprakasam. 2014. Axonal transport velocity estimation from kymographs based on curvilinear feature extraction and spline fitting. *In* 2014 36th Annual International Conference of the IEEE Engineering in Medicine and Biology Society IEEE, pp. 4240–4243.
38. Zinsmaier, K. E., M. Babic, and G. J. Russo. 2009. *In* Mitochondrial transport dynamics in axons and dendrites. Cell Biology of the Axon Springer, pp. 361–381.
39. Ligon, L. A., and O. Steward. 2000. Movement of mitochondria in the axons and dendrites of cultured hippocampal neurons. *J. Comp. Neurol.* 427:340–350.
40. Kapitein, L. C., M. A. Schlager, ..., C. C. Hoogenraad. 2010. Mixed microtubules steer dynein-driven cargo transport into dendrites. *Curr. Biol.* 20:290–299.
41. Kuznetsov, A. 2013. Modelling of axonal cargo rerouting in a dendrite. *Math. Med. Biol.* 30:273–285.
42. Karasmanis, E. P., C.-T. Phan, ..., E. T. Spiliotis. 2018. Polarity of neuronal membrane traffic requires sorting of kinesin motor cargo during entry into dendrites by a microtubule-associated septin. *Dev. Cell.* 46:518–524.
43. Rothman, J. S., L. Kocsis, ..., R. A. Silver. 2016. Physical determinants of vesicle mobility and supply at a central synapse. *Elife.* 5:e15133.
44. Schumm, R. D., and P. C. Bressloff. 2021. Search processes with stochastic resetting and partially absorbing targets. *J. Phys. Math. Theor.* 54:404004.
45. Kramers, H. A. 1940. Brownian motion in a field of force and the diffusion model of chemical reactions. *Physica.* 7:284–304.
46. Zhu, X., R. Hu, ..., I. Kaverina. 2015. Microtubules negatively regulate insulin secretion in pancreatic β cells. *Dev. Cell.* 34:656–668.
47. Rubinow, S., and J. Blum. 1980. A theoretical approach to the analysis of axonal transport. *Biophys. J.* 30:137–147.
48. Bressloff, P. C., and J. M. Newby. 2013. Stochastic models of intracellular transport. *Rev. Mod. Phys.* 85:135–196.
49. Nédélec, F., T. Surrey, and A. Maggs. 2001. Dynamic concentration of motors in microtubule arrays. *Phys. Rev. Lett.* 86:3192–3195.
50. Klumpp, S., T. M. Nieuwenhuizen, and R. Lipowsky. 2005. Self-organized density patterns of molecular motors in arrays of cytoskeletal filaments. *Biophys. J.* 88:3118–3132.